Systematic study of *p*-shell nuclei via single-nucleon knockout reactions

G. F. Grinyer,[1,2,*] D. Bazin,[2] A. Gade,[2,3] J. A. Tostevin,[2,4] P. Adrich,[2] M. D. Bowen,[2,3] B. A. Brown,[2,3] C. M. Campbell,[2,3] J. M. Cook,[2,3] T. Glasmacher,[2,3] S. McDaniel,[2,3] A. Obertelli,[2,†] K. Siwek,[2,3] J. R. Terry,[2,3] D. Weisshaar,[2] and R. B. Wiringa[5]

[1]*Grand Accélérateur National d'Ions Lourds (GANIL), CEA/DSM-CNRS/IN2P3, Bvd Henri Becquerel, 14076 Caen, France*

[2]*National Superconducting Cyclotron Laboratory, Michigan State University, East Lansing, Michigan 48824, USA*

[3]*Department of Physics and Astronomy, Michigan State University, East Lansing, Michigan 48824, USA*

[4]*Department of Physics, University of Surrey, Guildford, Surrey GU2 7XH, United Kingdom*

[5]*Physics Division, Argonne National Laboratory, Argonne, Illinois 60439, USA*

(Received 13 June 2012; published 29 August 2012)

A systematic investigation of the inclusive cross sections for single-nucleon knockout reactions from *p*-shell nuclei has been performed. A total of seven reactions were studied for projectiles with masses between $A = 7$ and 10, having a wide range of nucleon separation energies. Results were obtained for a range of incident beam energies and targets. These differences were found to have a minimal impact on the deduced cross sections. Experimental results were compared to theoretical predictions based on variational Monte Carlo (VMC) nuclear structure calculations, whose radial overlap functions and neutron and proton densities were included in the reaction description. These results are compared with the conventional model, developed for heavier nuclei, that uses shell-model and Hartree-Fock structure inputs. The VMC-based calculations agreed with the experimental data for several reactions where deeply bound nucleons are removed but does not describe some of the more weakly bound nucleon removal cases with comparable accuracy.

DOI: 10.1103/PhysRevC.86.024315 PACS number(s): 21.10.Jx, 21.60.De, 24.50.+g, 25.10.+s

I. INTRODUCTION

New insight into the complex structures of *p*-shell nuclei has recently been afforded through the combination of novel experimental techniques using rare-isotope beams and theoretical developments in nuclear structure calculations based on first-principles or *ab initio* approaches. Because these models do not rely on shell-model approximations, they offer a unique opportunity to study effects beyond truncated model space, effective interaction theories, including the role of three-body forces, pairing and continuum effects, clustering, and the influence of nucleon-nucleon (NN) correlations. For *p*-shell nuclei, in particular, tremendous theoretical progress has already been achieved using variational and Green's function Monte Carlo (VMC, GFMC) techniques [1] and the no-core shell model (NCSM) [2]. Comparisons to experimental measurements of electromagnetic transition rates [3], matter radii [4] and masses [5], and spectroscopic factors obtained from single-nucleon transfer reactions [6–8] and $(e, e'p)$ proton removal reactions [9] have all demonstrated effects that are not well described by the conventional shell model.

Single-neutron knockout reactions from intermediate-energy beams of ^{10}C and ^{10}Be on light nuclear targets have also demonstrated a sensitivity to differences in shell-model, NCSM, and VMC inputs to the reaction description [10] and so provide a complementary probe of wave functions that may assist the development of *ab initio* structure models. Previous analyses of proton knockout from the light and stable nuclei, ^{12}C and ^{16}O, showed that spectroscopic factors obtained from such knockout reactions were consistent with those derived from $(e, e'p)$ [11]. Because knockout reactions can probe both unstable nuclei and neutron configurations, not accessible with the $(e, e'p)$ technique, they offer a more general tool that can be applied across the entire *p* shell. The present study expands on the previous work by including several additional cases with projectile masses from $A = 7$ to 10 that span a wide range of nucleon separation energy. This provides a sufficiently large and diverse data set with which to perform a systematic study of the results of using VMC nuclear-structure inputs to compute the inclusive knockout reaction cross sections. These predictions are compared to those of the conventional shell model. A significant feature of the present work is the study of mirror symmetry using the two mirror reaction pairs (^{9}Li,^{8}Li)/(^{9}C,^{9}B) and (^{10}Be,^{9}Li)/(^{10}C,^{9}C). A detailed discussion of the experimental method and the theoretical analysis performed for these *p*-shell nuclei is presented.

II. EXPERIMENT

A summary of the reactions studied is provided in Table I. The data set consists of a total of 10 inclusive single-nucleon knockout cross-section measurements performed at intermediate energies ranging between 80 and 120 MeV/u and that employed different reaction target materials (Be or C). A result from a previous experiment on the proton knockout from ^{9}C [12] has also been included in the present data set and was reanalyzed according to the formalism described below. In the present experiment, secondary beams of ^{7}Li, ^{9}Li, ^{10}Be, and ^{10}C were produced following projectile fragmentation of an ^{16}O primary beam accelerated to 150 MeV/u in the K500 and K1200 coupled cyclotrons at the National Superconducting Cyclotron Laboratory (NSCL). Secondary beam energies of either 80 or 120 MeV/u were achieved by selecting between different thicknesses of the ^{9}Be primary production target (see

*grinyer@ganil.fr

†Present Address: CEA, Centre de Saclay, IRFU/Service de Physique Nucléaire, F-91191 Gif-sur-Yvette, France.

TABLE I. Summary of p-shell knockout reactions studied. The primary production targets were ^{9}Be. Secondary reaction targets were 188(2) mg/cm^2 [12] or 376(4) mg/cm^2 ^{9}Be or 403(5) mg/cm^2 ^{nat}C.

Initial state	Final state	Production target (mg/cm^2)	Projectile energy (MeV/u)	Secondary target (material)	σ_{exp} (mb)
^{7}Li	^{6}He	3526	80	Be	13.3(5)
^{7}Li	^{6}Li	2021	120	Be	30.7(18)
^{9}Li	^{8}Li	4113	80	Be	55.6(29)
		4113	80	C	62.9(41)
^{9}C	^{8}B	1763	100	Be	56.0(30)[a]
^{10}C	^{9}C	1034	120	Be	23.4(11)
		1034	120	C	27.4(13)
^{10}Be	^{9}Li	4113	80	Be	26.0(13)
^{10}Be	^{9}Be	1692	120	Be	71.2(40)
		4113	80	Be	69.5(32)

[a]Experimental result from Ref. [12].

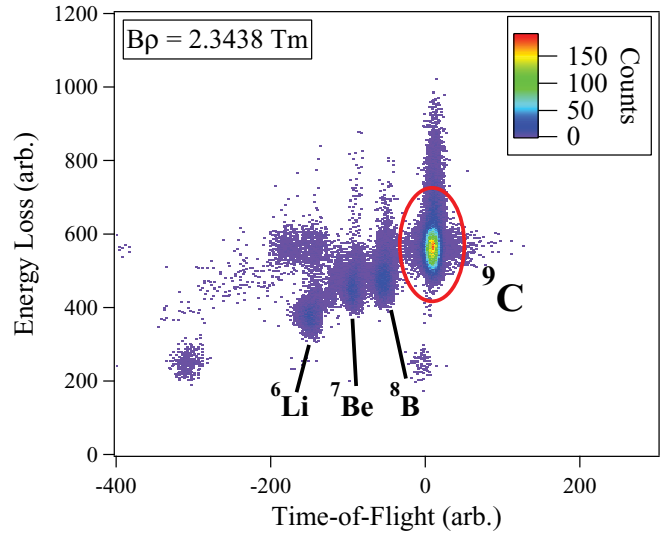

FIG. 1. (Color online) Particle-identification plot for reaction residues detected in the S800 focal plane at $B\rho = 2.3438$ Tm from a 120 MeV/u ^{10}C secondary beam on a ^{nat}C target.

Table I) that was located at the the entrance of the A1900 fragment separator [13]. The A1900 was operated with a momentum acceptance of $\Delta p/p = 1\%$ and a 450 mg/cm^2 Al wedge was placed at the intermediate image to purify the secondary beams based on their magnetic rigidity $B\rho$. Typical secondary-beam intensities of $\sim 10^5$ ions/s were then delivered to the experimental area and were impinged on reaction targets of either 376(4) mg/cm^2 ^{9}Be or 403(5) mg/cm^2 ^{nat}C located at the pivot point of the S800 spectrograph [14]. Secondary reaction products were identified on an event-by-event basis using the S800 focal-plane detection system that consisted of two x-y position-sensitive cathode read-out drift chamber (CRDC) detectors and followed by two large-area plastic scintillators of 3-mm and 5-cm thickness, respectively. The scintillators were used to determine the energy loss (ΔE) of the reaction residues passing through them and provided a start signal for a time-of-flight (TOF) measurement that was made relative to two thin (150 μm) plastic scintillators located 25 m upstream. An above-threshold signal from the 5-cm-thick scintillator was used to trigger the data acquisition. Trigger rates varied between 50 and 200 triggers/s that corresponded to data acquisition lives times of 90 and 75%, respectively. Inverse ray tracing of the particle trajectories through the 8-m flight path of the S800 was achieved using the ion-optics code COSY [15].

Identification of the single nucleon knockout residues in the S800 focal plane used the ΔE-TOF method of particle identification with the energy loss ΔE determined from the 5-cm-thick scintillator. A typical identification spectrum is provided in Fig. 1 for a ^{10}C beam at 120 MeV/u on the ^{nat}C reaction target with a S800 magnetic rigidity setting of $B\rho = 2.3438$ Tm for the ^{9}C residues. The resolution was clearly sufficient to unambiguously distinguish the single nucleon knockout residues from other reaction products. Longitudinal-momentum distributions for light nuclei are relatively wide, with $\Delta p/p \sim 15\%$, compared to the $\pm 2.5\%$ momentum acceptance of the S800 spectrograph [14]. In order to measure the entire longitudinal-momentum distribution for each reaction, it was, therefore, necessary to collect data at several overlapping magnetic rigidities by adjusting the $B\rho$ of the S800 in incremental steps of $\sim 2\%$. Between every change in magnetic rigidity, the dipoles of the S800 were first retuned to the unreacted setting (the $B\rho$ corresponding to the incident beam) in order to provide independent measurements of the secondary beam intensity, purity, and overall transmission to the focal plane. Knockout data were collected at each rigidity setting for ~ 2 h, while the unreacted beam runs between knockout settings were typically ~ 10 min each. The difference in the magnetic field between the reacted and unreacted beam runs was of order $\sim 10\%$ and internal NMR probes ensured that the dipoles had stabilized after each change in magnetic rigidity and before any data were collected. Reconstruction of the total momentum distribution, for each knockout residue, was then performed in software using the relative normalizations obtained from the total number of counts collected in the upstream scintillator for each run. The absolute normalization of the entire distribution was fixed using the data collected during the unreacted beam settings. A rigidity-dependent correction was then applied in the final stage of the analysis to account for the different live times of the data acquisition and the systematic losses associated with the angular acceptance of the spectrograph (described in detail below). An example of this reconstruction procedure is shown in Fig. 2 for ^{6}He residues following the proton knockout from an incident ^{7}Li beam. Other examples can be found in Fig. 1 of Ref. [10] for neutron knockout from ^{10}C and ^{10}Be. It should be emphasized that the excellent agreement in terms of the relative normalizations for each magnetic rigidity segment do not rely on any fitting procedure or include any free parameters. This provided an important and necessary consistency check of the analysis procedure.

Corrections to the experimental longitudinal-momentum distributions were required to determine the absolute cross sections and these arose primarily from three sources. The efficiencies of the CRDC detectors were determined on a run-by-run basis from the ratio of the total number of reconstructed

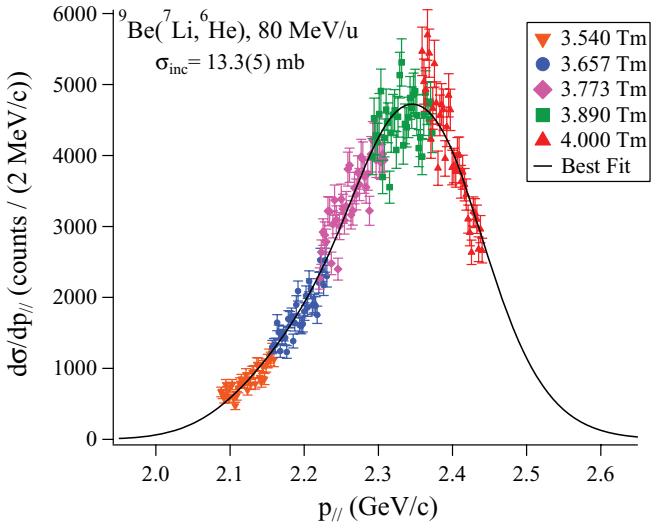

FIG. 2. (Color online) Longitudinal-momentum distribution for ^{6}He proton knockout residues (from an incident ^{7}Li beam at 80 MeV/u) reconstructed from data collected at five overlapping magnetic rigidities. An eikonal-plus-Gaussian fit (solid line) was used to deduce the unobserved cross section in the tails of the distribution.

events that require a coincidence event between both CRDC detectors to the total number of trigger (singles) events in the 5-cm-thick focal-plane scintillator. This resulted in a 3% correction that was applied to the experimental distributions and was found to be relatively constant throughout the course of the experiment. A second correction was required to account for the dead time of the data acquisition and this was determined on a run-by-run basis by comparing two scalers counting identical outputs from a common pulse generator. One of the outputs of the pulse generator was sent directly to a scaler module, while the other output was, first, vetoed during the acquisition busy and then sent to an identical scaler. Dead-time corrections applied to the raw data varied between 10 and 25% depending on the particular reaction and magnetic rigidity settings used.

The third, and most significant, correction was required to account for losses associated with the finite angular acceptance of the S800 that is limited to $\pm 3.5^{\circ}$ and $\pm 5.0^{\circ}$ in the dispersive and nondispersive directions, respectively [14]. As the scattering angles of the reaction products are inversely proportional to their momentum, these corrections were maximal for the lightest mass residues at the lowest-incident beam energy. The most extreme case was that of proton knockout from ^{7}Li at 80 MeV/u, where the acceptance losses are clearly visible in Fig. 3, particularly in the dispersive direction. The angular acceptance losses were observed to vary as a function of magnetic rigidity within a given reaction (see Fig. 3) with the smallest values of $B\rho$ (the lowest momentum) requiring the largest corrections.

A correction procedure was developed to account for these rigidity-dependent losses that was based on the comparison of the experimental data to the transverse-momentum distributions expected theoretically as described in Ref. [16]. The theoretical transverse-momentum distributions were obtained using the same S matrices and input parameters that were used in the derivation of the single-particle cross sections described below. While these calculations were able to reproduce the approximate widths of the experimental transverse-momentum distributions, they do not account for the observed variation of this width with magnetic rigidity. It was, therefore, necessary to match the widths of the theoretical distributions (and their overall normalizations) to the experimental data for scattering angles less than 3.5° in both the dispersive and nondispersive directions. Below 3.5°, angular-acceptance losses were assumed to be negligible. With the width and normalization factors applied, the tails of the theoretical distribution (for angles larger than 3.5°) were then compared to the experimental distributions at each magnetic rigidity in order to estimate the fraction of the data lost. An example of this procedure is shown in Fig. 4 for the case of ^{9}C reaction residues following single neutron knockout from an incident beam of ^{10}C at 120 MeV/u. The difference between the normalized theoretical and symmetric eikonal distribution [Fig. 4(a)] and the experimental data [Fig. 4(b)] gives rise to an annular distribution [Fig. 4(c)] that was used to estimate the fraction of events lost. For the data shown in Fig. 4, the ratio of the counts in the annulus to the total number of counts is $9 \pm 6\%$. For the most extreme case of the ^{6}He residues shown in Fig. 3, angular-acceptance corrections of $34 \pm 7\%$, $27 \pm 6\%$, and $15 \pm 6\%$ were determined at 3.657, 3.773, and 4.000 Tm, respectively. The uncertainties on the correction factors are dominated by a $\pm 5\%$ uncertainty that was conservatively estimated to reflect any potential systematic bias introduced by this procedure.

With these corrections applied to the raw experimental data, the inclusive cross section was then determined from a fit to the longitudinal-momentum distribution (see, for example, the solid line in Fig. 2). The fit function was composed of a combination of the expected eikonal shape (see below) with a Gaussian distribution that was required to account for the commonly observed extended tail at low momenta caused by dissipative, stripping events in the target [17,18]. A fit function, rather than direct integration of the corrected data, was required to account for the cross section in the low- and high-momentum tails of the experimental distributions and that were not observed in the experiment. In principle, these data could have been measured by selecting even further steps in magnetic rigidity. However, as their contribution to the inclusive cross section is rather small (less than 10% for all reactions studied), it follows that a significant amount of the total experimental time would have been required to acquire these data. The number of rigidity steps for each reaction were, thus, optimized to collect as much of the experimental distribution as possible while leaving sufficient time to maximize the number of reactions that could be studied in the experiment. The example of Fig. 2, represents the only reaction studied where it was not possible to measure an additional rigidity step on the high-momentum side due the 4.0-Tm restriction of the S800 spectrograph.

Experimental inclusive momentum distributions and their corresponding best-fit distributions for several of the reactions studied in this work are presented in Fig. 5. We observe that the measured (^{10}Be,^{9}Li) momentum distribution at the lower beam energy, 80 MeV/u, Fig. 5(c), for removal of the

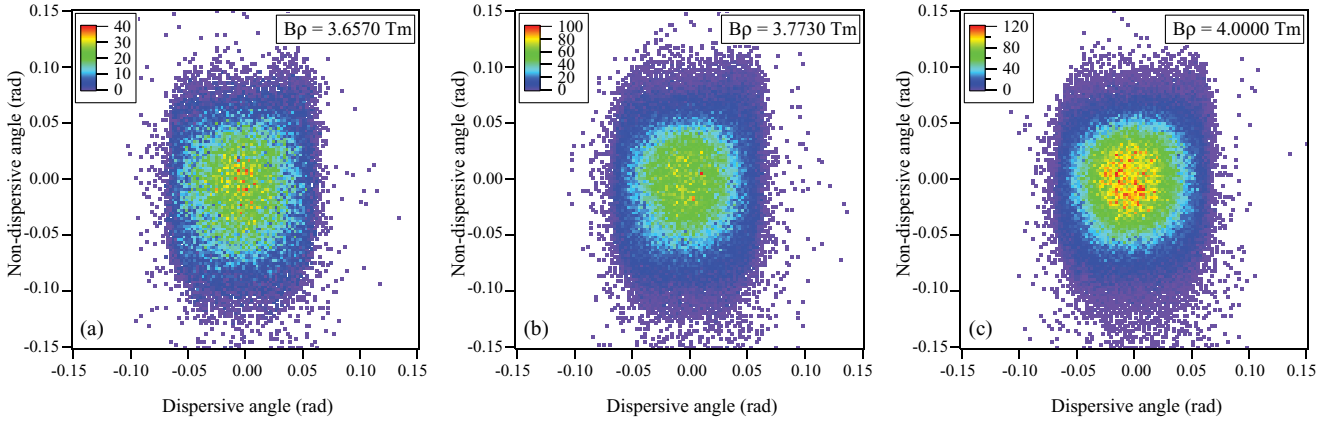

FIG. 3. (Color online) Nondispersive versus dispersive angular plots for ^{6}He proton knockout residues (incident ^{7}Li beam at 80 MeV/u) measured at three settings of the magnetic rigidity (indicated). The vertical cut displayed in the data at ± 0.06 rad (± 3.5°) corresponds to the angular acceptance of the S800 spectrograph in the dispersive direction [14].

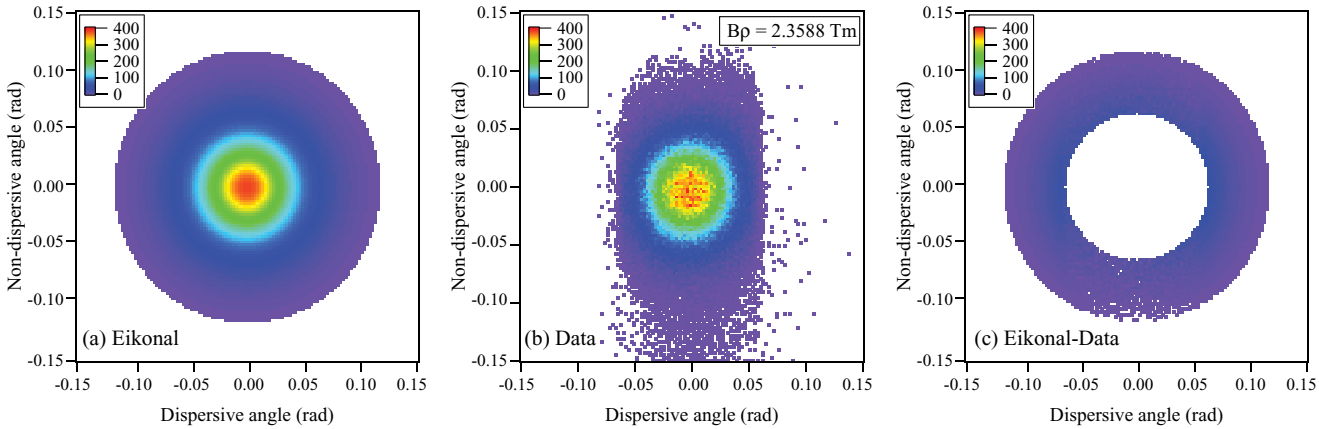

FIG. 4. (Color online) Nondispersive versus dispersive angular plot (b) for ^{9}C neutron knockout residues (incident ^{10}C beam at 120 MeV/u) measured at the magnetic rigidity $B\rho = 2.3588$ Tm. (a) Theoretical prediction, normalized to the experimental data, assuming no angular acceptance losses. (c) The difference between the theoretical and experimental data (for angles larger than 3.5°) was used to determine the acceptance correction to be applied to the data.

most bound proton with $S_p \approx 20$ MeV, shows evidence in its high-momentum tail of the energy-momentum conservation imposed cutoff on the allowed momenta of the forward-travelling residue. Kinematics place this limit at a momentum of 137 MeV/c above the peak position of the distribution in this case. The highest-momentum data points are consistent with a sharply cut-off eikonal distribution and the experimental momentum resolution, which is of order 1%. Based on the eikonal momentum distribution, this kinematics cutoff suggests a 10% reduction in the predicted theoretical yield. A more dramatic example of this kinematics effect has been seen in a recent strongly bound nucleon removal data set taken using a lower-energy beam [19]. The (^{10}C,^{9}C) mirror reaction at 120 MeV/u, the lower right panel, where the neutron separation energy is 21.3 MeV, shows no such effect, as is expected from a kinematics calculation at this higher energy. Inclusive cross sections derived from the integral of the best-fit functions and results, for all reactions, are those provided in Table I.

III. EIKONAL REACTION MODEL

Single-nucleon knockout refers to direct reactions in which a nucleon is removed from near the surface of a fast-moving projectile in a collision with a light target nucleus. For such fast surface-grazing collisions the reaction dynamics can be calculated, making use of the sudden and eikonal approximations [20–22] that are appropriate for high-energy projectiles and reactions dominated by small-angle scattering and forward traveling reaction products [22]. Within the eikonal model, theoretical cross sections $\sigma_{\rm th}(I^{\pi})$ for the removal of a single nucleon with spherical quantum numbers (n, l, j) from a projectile with mass number A, producing the mass $A-1$ residue in a final state I^{π} at an excitation energy E_x, can be expressed as

$$\sigma_{\rm th}(I^{\pi}) = \left(\frac{A}{A-1}\right)^{N} C^2 S(I^{\pi}, j)\sigma_{\rm sp}(j^{\pi}, S_n + E_x). \quad (1)$$

Here S_n is the ground-state-to-ground-state nucleon separation energy and $S_n + E_x$ is the effective separation energy to

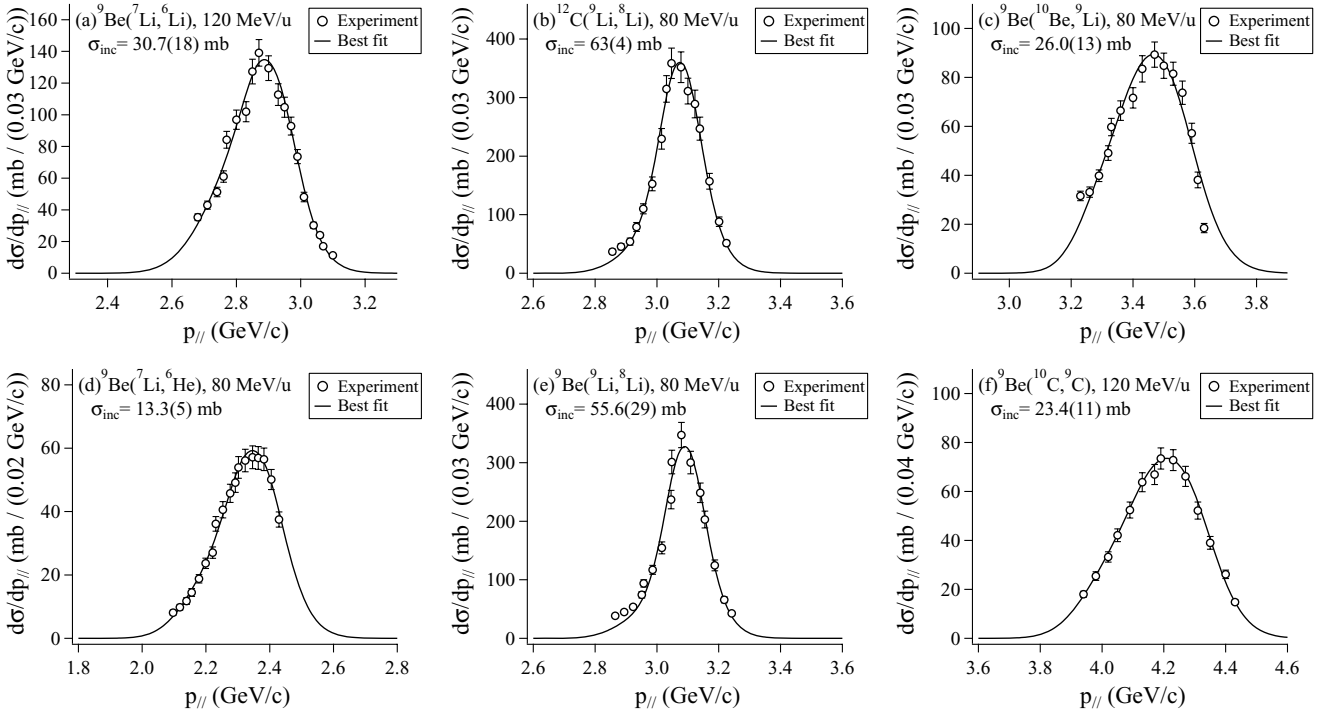

FIG. 5. Inclusive longitudinal-momentum distributions for a selection of reactions studied in this work. The best fits (solid curves) are the sum of a component with the shape of the calculated eikonal model distribution and a Gaussian distribution. Experimental inclusive cross sections, obtained by integrating the best-fit distributions, are also indicated.

the populated excited state. The center-of-mass correction factor, $[A/(A-1)]^N$, with $N = 1$ for p-shell nuclei, is applied when using shell-model spectroscopic factors C^2S [22]. The inclusive cross sections are the sums of these $\sigma_{\rm th}(I^\pi)$ for all particle-bound final states. The single-particle cross sections $\sigma_{\rm sp}$ are the sums of independent calculations for the stripping and diffractive nucleon removal mechanisms. Stripping, or inelastic breakup, is the dominant contribution to the single-particle cross section. It describes events where the removed nucleon interacts inelastically with the target exciting it from its ground state. The diffractive or elastic component accounts for events that remove a nucleon from the projectile via an elastic interaction with the target. Through an exclusive measurement that also detected the removed protons following proton knockout reactions from ^{9}C and ^{8}B, it was demonstrated that this reaction model successfully described the relative contributions of the stripping and diffractive mechanisms to the inclusive cross sections [12].

These stripping and diffractive component calculations require consistent, reaction specific, nuclear structure inputs of two types: (i) The point neutron and proton densities of the mass $A-1$ residual nuclei, used to generate the residue-target elastic S matrices, and (ii) the projectile and residue nucleus single-nucleon overlap functions, computed from their A- and $(A-1)$-body wave functions. The nucleon-target S matrices are calculated using an assumed (generic) target density, and so the S matrices are common to all reactions on a given target at a given energy. The densities of the ^{9}Be and ^{12}C target nuclei were assumed to be of Gaussian form with root-mean-square (rms) radii of 2.36 and 2.32 fm, respectively, for all the reactions. The strength of the NN effective interaction used to construct the S matrices was modified from the free neutron-neutron and neutron-proton cross sections, the real-to-imaginary ratios of the NN forward-scattering amplitudes being interpolated (using a polynomial fit) from the values tabulated by Ray [23].

The emphasis here is to take these two structure inputs from microscopic VMC calculations, which have been computed for all of the p-shell systems measured. For comparison purposes we also show the results when using the more conventional shell-model approach, as has been used for more massive projectiles where fully microscopic calculations are, as yet, not available. We first outline this more commonly used approach. It should also be pointed out that the factorization of the single-nucleon overlaps made in Eq. (1), to give a spectroscopic factor and a single-particle cross section computed with a normalized radial wave function, while natural for the shell-model approach is simply one of convenience for the VMC overlaps. We choose to continue to separate the overlap function and its norm (the spectroscopic factor) in this way to assist in our discussion of the dominant changes introduced when using the VMC and their origin in terms of the overlap strengths (the spectroscopic factors) and their geometries (their rms radii), as will be discussed below.

A. Shell-model approach

As in analyses for heavier projectile nuclei [24], the following nuclear structure information was used. (a) The

residues' point neutron and proton densities were obtained from spherical Hartree-Fock calculations using a Skyrme force (the SkX interaction [25]). (b) The projectile and residue overlap functions were obtained from the shell model, i.e., their spectroscopic factors, and their radial form factors were described by normalized eigenstates of a Woods-Saxon plus spin-orbit potential well with the depth constrained by the experimental $S_n + E_x$ of Eq. (1). A fixed diffuseness parameter, of 0.7 fm, and spin-orbit interaction strength, of 6.0 MeV, were assumed throughout. The radius parameters of the Woods-Saxon wells, $r_{\rm SM}$, were determined from a fit to the rms radius of each nucleon single-particle orbital of interest, as calculated by the HF-SkX calculation. Because the rms radius of the nucleon's overlap wave function, $R_{\rm SM}^{\rm olap}$, plays a significant role in the determination of the single-particle cross section, see below and also Ref. [24], its value must be consistently specified. Hence, our use of the same theoretical (HF) model to constrain this radius as was used to compute the densities required for the S-matrix evaluations. Our choice of the SkX Skyrme interaction was motivated by it having been fitted to a large body of data, including measured binding energies, charge radii, and single-particle energies [25], and its success in reproducing properties related to the nuclear size, such as proton and neutron densities [26] and high-energy interaction cross sections [27].

For completeness, the deduced Woods-Saxon radius parameters, $r_{\rm SM}$, the corresponding single-nucleon overlap rms radii, $R_{\rm SM}^{\rm olap}$, and the core/residual nuclei rms radii $R_{\rm SM}^{\rm core}$ are collected in Table II. The single-particle cross sections derived from these shell-model (SM) inputs are also shown as $\sigma_{\rm SM}^{\rm sp}$. We reiterate that these calculations are presented largely for comparative purposes since, for the mass $A \leqslant 10$ systems under investigation, aspects of the models used, for example, the HF mean field, are at the limits of their applicability.

B. Variational Monte Carlo approach

We now discuss the corresponding cross section calculations when taking the nuclear structure inputs from quantum variational Monte Carlo calculations. The VMC method, detailed below, provides state-of-the-art microscopic wave functions in these light p-shell nuclei, calculations being feasible presently up to ^{12}C. The VMC many-body wave functions are used to provide a revised and consistent set of microscopically derived residue densities and nucleon overlaps, expected to be superior to those of the truncated-space shell model. Comparison between the two methods is nevertheless valuable in assessing the changes in spectroscopy and geometry that arise, which help determine the significance of remaining deviations from the measured cross sections.

The VMC calculations were based on the Argonne v_{18} (AV18) two-body interaction [28]. As realistic two-nucleon forces are known to be insufficient for reproducing certain physical observables such as nucleon binding energies [1], the addition of three-body interactions such as Urbana-IX (UIX) [29] or Illinois-7 (IL7) [30,31] are required. Recent GFMC calculations using AV18 + IL7 are able to reproduce the experimental binding energies at the level of 1% [31] for $A \leqslant 7$ nuclei. In terms of binding energies, full GFMC calculations are essential as their initial starting-point trial wave functions (these are the same wave functions that are used in the less computationally intensive VMC calculations) typically miss approximately 1.5 MeV for each nucleon added to the p shell [1]. This well-known binding-energy problem leads, for example, to the calculated VMC ground states of ^{6}Li and ^{6}He being unstable with respect to $\alpha + d$ and $\alpha + 2n$ breakup, respectively.

Whether the VMC calculations exactly reproduce experimental binding and separation energies is not a primary concern for our knockout reactions analysis. In all cases,

TABLE II. Bound-state Woods-Saxon potential parameters r, a, separation energies ($S_E = S_n + E_x$), final-state spins I^π, and total angular momenta j of the removed nucleon for each transition in the reactions set studied. The calculated rms radii of the residual nuclei ($R^{\rm core}$) and wave-function overlaps ($R^{\rm olap}$) and the resulting single-particle cross sections $\sigma^{\rm sp}$ are shown for both the shell-model (SM) and variational Monte Carlo (VMC) structure inputs to the reaction calculations. In all SM calculations, $a_{\rm SM}$ was fixed at the value 0.7 fm.

Reaction	Energy (MeV/u)	I^π	S_E (MeV)	j	$R_{\rm SM}^{\rm core}$ (fm)	$R_{\rm VMC}^{\rm core}$ (fm)	$r_{\rm SM}$ (fm)	$r_{\rm VMC}$ (fm)	$a_{\rm VMC}$ (fm)	$R_{\rm SM}^{\rm olap}$ (fm)	$R_{\rm VMC}^{\rm olap}$ (fm)	$\sigma_{\rm SM}^{\rm sp}$ (mb)	$\sigma_{\rm VMC}^{\rm sp}$ (mb)
(^{7}Li,^{6}He)	80	0^+	9.98	3/2	2.40	2.55	1.34	1.37(9)	1.18(7)	2.75	3.23(8)	48.5	60.8(31)
(^{7}Li,^{6}Li)	120	1^+	7.25	1/2	2.08	2.40	1.32	1.45(8)	0.95(6)	2.90	3.27(8)	50.1	56.8(26)
				3/2			1.27	1.486(32)	0.910(32)	2.90	3.28(4)	50.0	56.9(13)
		0^+	10.8	3/2	2.08	2.57	1.27	1.37(9)	1.22(7)	2.68	3.22(8)	43.7	54.1(25)
(^{9}Li,^{8}Li)	80	2^+	4.06	1/2	2.31	2.40	1.24	1.706(21)	0.519(32)	3.25	3.45(6)	52.0	55.7(21)
				3/2			1.19	1.350(17)	0.606(25)	3.26	3.30(4)	52.3	50.6(11)
		1^+	5.05	3/2	2.31	2.43	1.19	1.349(21)	0.678(28)	3.12	3.24(4)	47.6	48.0(12)
(^{9}C,^{8}B)	100	2^+	1.30	3/2	2.38	2.40	1.11	1.313(20)	0.532(28)	3.54	3.51(4)	61.3	58.0(15)
				1/2				1.688(16)	0.401(29)		3.63(4)		62.2(14)
(^{10}Be,^{9}Be)[a]	120	$\frac{3}{2}^-$	6.81	3/2	2.27	2.46	1.24	1.25(6)	0.79(7)	3.02	3.12(9)	39.0	37.7(24)
(^{10}Be,^{9}Li)	80	$\frac{3}{2}^-$	19.64	3/2	2.36	2.41	1.34	1.35(9)	1.15(12)	2.54	2.84(10)	28.1	34.8(29)
		$\frac{1}{2}^-$	22.33	1/2	2.36	2.44	1.41	1.56(6)	0.95(10)	2.50	2.78(7)	27.0	32.3(20)
(^{10}C,^{9}C)[a]	120	$\frac{3}{2}^-$	21.28	3/2	2.45	2.50	1.36	1.46(7)	1.11(11)	2.55	2.86(8)	24.9	31.5(20)

[a]Some of the SM potential parameters were incorrectly transcribed in Table II of Ref. [10]. The corrected values are shown here.

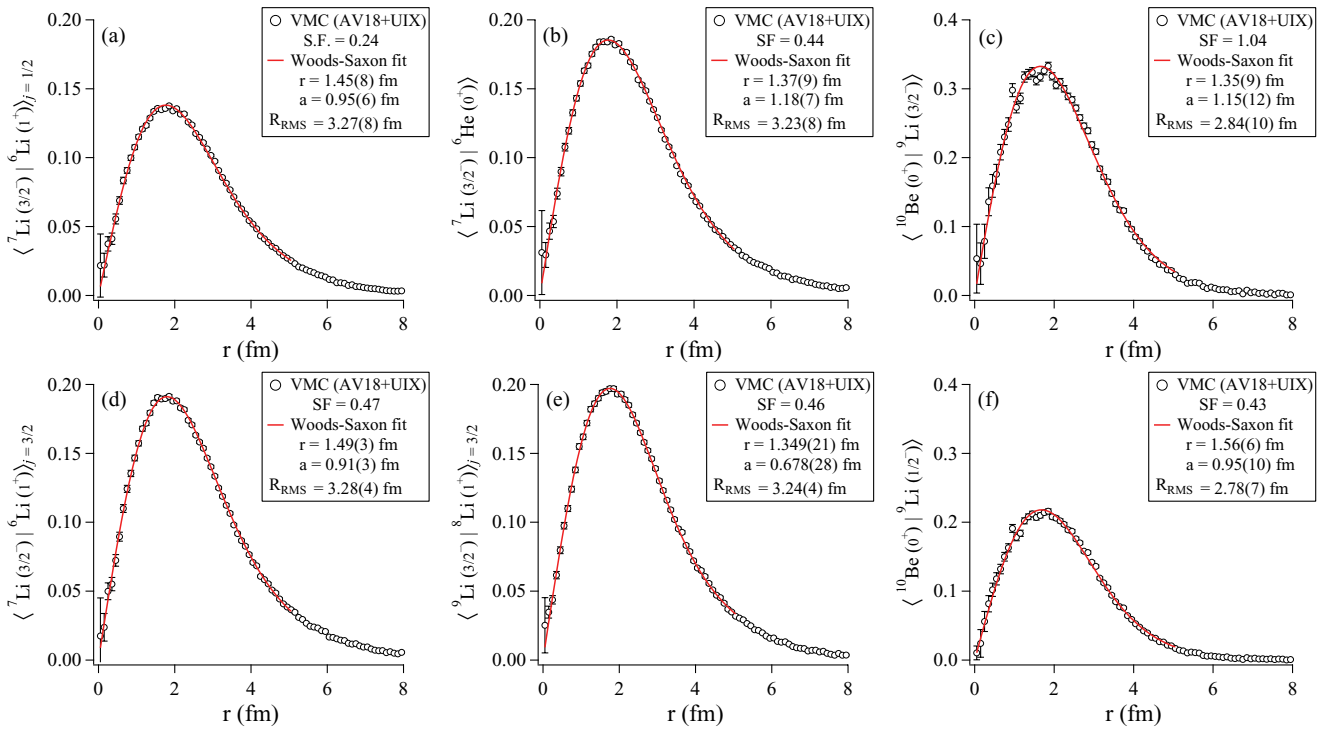

FIG. 6. (Color online) Radial forms of the VMC wave-function overlaps (open points) and of the Woods-Saxon wave functions calculated with radius r_{VMC} and diffuseness a_{VMC} parameters obtained from a best fit (solid line). The VMC-model spectroscopic factors (SF), i.e., the norms of the VMC and the fitted radial overlaps, are also indicated.

Woods-Saxon eigenstate representations (fits) to the numerical VMC overlaps are constrained by the known *experimental* separation energies. However, it is important that the calculations demonstrate reasonable quantitative agreement with spectroscopic quantities and observables related to the nuclear size. In this regard, the VMC and GFMC results are nearly equivalent. Differences of typically 10% and less have been obtained on quantities such as spectroscopic factors and asymptotic normalization coefficients (ANC) [31,32] and the VMC wave functions are constrained to reproduce available rms radii [1]. For example, good agreement has been obtained between VMC and GFMC calculations for experimental measurements of charge radii in ^{6}He and ^{8}He [4], spectroscopic factors obtained from low-energy nucleon transfer [6–8] and high-energy $(e, e'p)$ reactions [9], charge radii and electromagnetic moments in $A \leqslant 9$ Li isotopes [33], and electromagnetic form factors [34].

As was detailed earlier, two structure inputs are needed to incorporate the VMC model into the reaction formalism. The first inputs are the point nucleon densities of the residual nuclei, used to compute the residue-target S matrices. The VMC numerical values are used. Because the VMC densities are constrained to reproduced available experimental rms radii [1], we neglect the uncertainties on these residue rms radii in comparison with those on the VMC overlap functions, that are discussed in detail below. These VMC rms matter radii of the residues, $R^{\mathrm{core}}_{\mathrm{VMC}}$, are collected in Table II. The second inputs are the single-nucleon radial overlaps. As was already indicated, not all of the computed VMC overlaps have the correct physical separation energy and, hence, do not have the correct large-r asymptotic forms. We adopted the following procedure. Each numerical VMC radial overlap was fitted by an eigenstate in a Woods-Saxon potential well, the eigenstate having the required empirical separation energy and the same normalization (SF) as that of the VMC. Each fit required the determination of radius and diffuseness parameters, r_{VMC} and a_{VMC}. These Woods-Saxon parameters and the separation energy then determine the rms radius of the fitted VMC overlap, $R^{\mathrm{olap}}_{\mathrm{VMC}}$, the key component in the determination of the single-particle cross sections. Several representative overlap fits are shown in Fig. 6 and all results are provided in Table II. Following the discussion above, and also in Ref. [32], since the radial forms of the VMC overlaps may not have the correct asymptotic form, only that part of the overlap from 0 and 5 fm was used for the fit and the determination of its uncertainties. The sensitivity of our deduced Woods-Saxon parameters to this particular choice of radius was investigated by fitting the overlaps from the origin out to different maximum radii. The details of these fits are reaction dependent. An example is shown in Fig. 7 for the case of the $\langle {}^{10}\mathrm{Be}|{}^{9}\mathrm{Be}+n\rangle$ overlap, where both the fitted Woods-Saxon parameters and the deduced rms radius of the overlap, $R^{\mathrm{olap}}_{\mathrm{VMC}}$, are seen to be essentially independent of the radial cutoff used. Statistical uncertainties on the fitted well parameters r_{VMC} and a_{VMC} naturally arise from the fact that the VMC overlaps are Monte Carlo generated. Uncertainties on the overlap rms radii $R^{\mathrm{olap}}_{\mathrm{VMC}}$ and single-particle cross sections $\sigma^{\mathrm{sp}}_{\mathrm{VMC}}$ were obtained by varying the r_{VMC} and a_{VMC} values by 1 standard deviation in the reaction-model calculations and combining the absolute differences from each in quadrature.

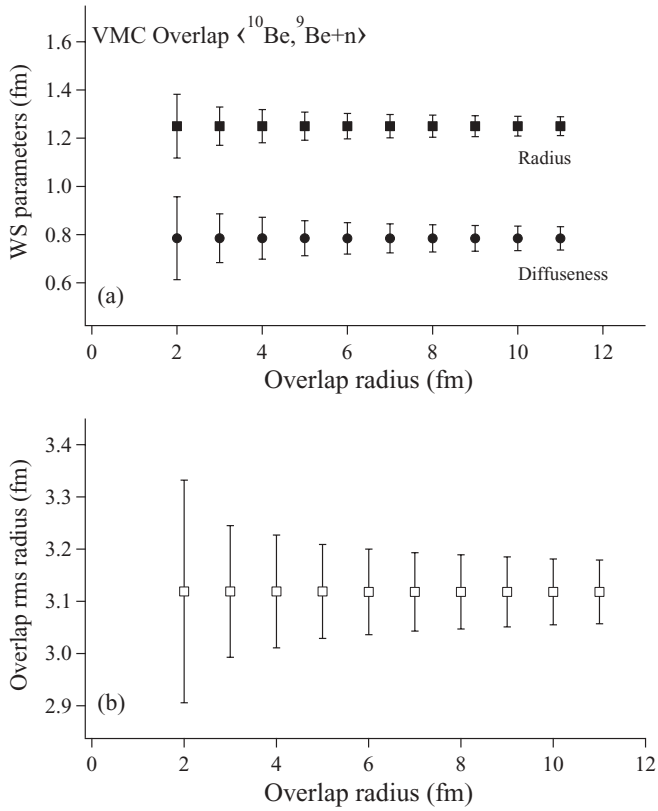

FIG. 7. Woods-Saxon parameters and VMC overlap rms radius for $\langle^{10}\mathrm{Be}|^{9}\mathrm{Be}+n\rangle$ as a function of the maximum radius used in the fit to the numerical VMC values. The final fitted results and their uncertainties were computed for $r = 5$ fm (see text).

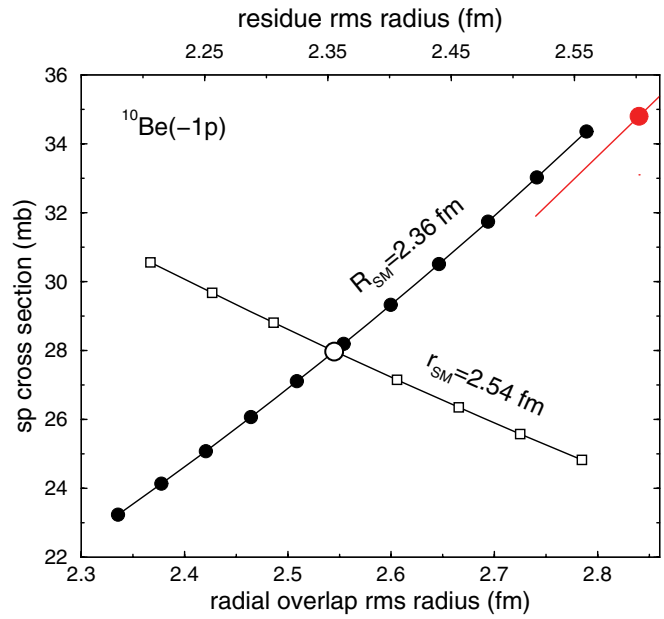

FIG. 8. (Color online) Variation of the calculated single-particle cross sections with the assumed residue (open squares and upper scale) and single-nucleon overlap (solid points and lower scale) rms radii, for proton removal from ^{10}Be to ^{9}Li ($j^{\pi} = \frac{3}{2}^{-}$). The (red) point and error bar correspond to the VMC single-particle cross section and orbital rms radius. The open circle shows the corresponding SM/HF-SkX values.

Before comparing the experimental and VMC theoretical inclusive cross sections, that also involve the spectroscopic factors, it is useful for understanding the final cross sections to discuss the sensitivities of the single-particle cross sections shown in Table II. These sensitivities originate essentially from the structure-model-generated geometry rather than the spectroscopy of the reaction. Specifically, being surface dominated, the reactions are sensitive to the relative sizes of (a) the residual nucleus (that controls the radius at which strong absorption sets in and that leads to more complex channels) and (b) the removed nucleons' orbital motion in the projectile (that controls the probability for finding the nucleon outside of the region of strong absorption) that determines the removal reaction yield. The single-particle cross sections of Table II are correlated with these two sizes. This sensitivity is illustrated in Fig. 8 for the case of proton removal from ^{10}Be populating the $\frac{3}{2}^{-}$ ground state in ^{9}Li. Non-VMC-model calculations are used to allow variations of the residue and orbital sizes. The open circle, at the intersection of the two lines, reflects the $\sigma^{\mathrm{sp}}_{\mathrm{SM}}$ for the $R^{\mathrm{core}}_{\mathrm{SM}} = 2.36$ fm and $R^{\mathrm{olap}}_{\mathrm{SM}} = 2.54$ fm values of Table II. With the ^{9}Li rms radius $R^{\mathrm{core}}_{\mathrm{SM}}$ kept fixed, the solid points show the (essentially linear) cross-section variation with the rms size of the $\frac{3}{2}^{-}$ orbital (lower scale), more extended orbitals driving increased reaction yields. If the $\frac{3}{2}^{-}$ orbital rms radius $R^{\mathrm{olap}}_{\mathrm{SM}}$ is kept fixed (at 2.54 fm), the open square points show the (essentially linear) cross-section variation with the rms size of the residue (upper scale), with larger residues suppressing reaction yields. A theoretically consistent derivation of these two radii is, thus, of considerable importance for the calculated cross sections. The red point (upper right) shows the VMC $\sigma^{\mathrm{sp}}_{\mathrm{VMC}}$ value. Its error bar is correlated with the deduced uncertainty in $R^{\mathrm{olap}}_{\mathrm{VMC}}$. The point lies to the right of the $R^{\mathrm{core}} = 2.36$ fm line, as expected given that $R^{\mathrm{core}}_{\mathrm{VMC}} = 2.41$ fm. Table II shows that the single-particle cross sections derived from VMC are, in most cases, larger than those of the HF-SkX methodology. This reflects, primarily, the generally increased rms radii of the VMC overlaps. The cross section changes are moderated in several cases by differences in the residue rms radii from the VMC and HF-SkX calculations. The differences in the tabulated cross sections can therefore be understood with reference to the dependencies shown in Fig. 8.

We note that there are some significant differences between the rms radii of both residues, given by the VMC, and the single-nucleon overlaps, which we have fitted to the VMC, and those obtained from the Hartree-Fock-constrained approach. As was hinted earlier, these light projectiles have not yet established a well-developed mass $A-1$ core of nucleons and are not expected to be well-described in the mean-field limit. The results presented in Table II reinforce this view strongly. This observation also has implications for the reaction model used, which leads to Eq. (1) and which assumes that the residual nucleus (the nonremoved nucleons) act as spectators and are not affected dynamically or excited during the collision. The validity of this approximation is untested for such light systems. To do so will almost certainly

require exclusive final-states data and the generalization of the theoretical framework used here.

IV. RESULTS AND DISCUSSION

The single-particle cross sections of Table II, calculated using the formalism described in Sec. III, were combined with the spectroscopic factors from the nuclear-structure models to compute the theoretical cross sections using Eq. (1). The VMC spectroscopic factors are given by the norms of the VMC overlap functions. For the shell-model overlaps, spectroscopic factors were calculated using the the Cohen-Kurath POT (CKPOT) effective interaction [35]. Comparisons of the theoretical and experimental inclusive cross sections are presented below, ordered with increasing mass number of the incident projectiles.

A. Knockout reactions from $A = 7$

The lightest nuclei investigated were from neutron and proton knockout from a ^{7}Li beam at 120 and 80 MeV/u, respectively. The initial motivation for studying these cases was driven by the existing data from the ^{7}Li$(e, e'p)^6$He reaction and its comparison to VMC calculations [9]. However, these cases turned out to be the most challenging, both experimentally and in the applicability of the eikonal reaction model. For neutron knockout to ^{6}Li the inclusive cross section was 30.7(18) mb, obtained from the fit shown in Fig. 5. The lower beam energy for the proton knockout reaction was required to ensure that the magnetic rigidity of the ^{6}He residues did not exceed the 4.0-Tm limitation of the S800 spectrograph. Thus, proton knockout to ^{6}He offered the most significant experimental challenge as, with the reduction in beam energy coupled with the fact that it was the lightest case studied, there were appreciable losses due to the angular acceptance of the spectrometer. As described in Sec. II, these corrections amounted to 15% at central rigidities and up to 35% in the low-momentum tail. The experimental inclusive cross section was 13.3(5) mb. This is one of the smallest cross sections that has been measured for a single-nucleon knockout reaction. Most likely this reflects the structural differences between the ^{7}Li ground state, having a significant α-plus-triton cluster component, and the weakly bound two-neutron halo-like ground-state configuration in ^{6}He. From the perspective of the reaction model, these $A = 7$ knockout reactions are also challenging. The reaction model assumption that the residual nucleons act as a spectator and are not dynamically excited during the collision is a particular issue for the ^{6}He residue that is weakly bound and easily dissociated. The expectation is that theory will overestimate the proton removal cross section. Coupling to ^{6}He breakup channels is missing from the formalism and also from the ^{6}He-target S matrices used presently, so the ^{6}He ground-state survival probability is expected to be overestimated.

The theoretical cross sections for proton and neutron removal from ^{7}Li are shown in Table III. In the proton knockout only the ^{6}He(0^+) ground state is bound and the theoretical cross sections to this state are 27 and 39 mb using the VMC and SM approaches, respectively. The main source of this difference is the spectroscopic factor, 0.439 and 0.806, from the respective models. The VMC cross section is larger than the experimental value of 13.4(7) mb by about a factor of 2. As described above, the well-known few-body-like dynamics of these lightest nuclei are absent from the spectator-core assumption of the reaction model, as currently formulated, and so do not allow quantitative conclusions to be drawn.

TABLE III. Comparison of theoretical and experimental inclusive cross sections for knockout reactions from $A = 7$ projectiles. The spectroscopic factors (SF) from shell-model include the 1.17 center-of-mass motion correction.

Reaction	Final state	SF CKPOT	SF VMC	σ_{th}^{SM} (mb)	σ_{th}^{VMC} (mb)	σ_{exp} (mb)
(^{7}Li,^{6}He)	0^+	0.806	0.439	39.1	26.7(14)	
Inclusive				39.1	26.7(14)	13.4(7)
(^{7}Li,^{6}Li)	1^+	0.733	0.715	36.8	40.7(9)	
	0^+	0.389	0.219	17.0	11.9(5)	
Inclusive				53.8	52.6(10)	30.7(18)

For neutron knockout to ^{6}Li the theoretical inclusive cross sections were obtained assuming that only the 1^+ ground state and the 0^+ excited state at 3.5 MeV were populated in the reaction. An additional (3^+, 2.2 MeV) excited state is known but is particle unbound and decays by $\alpha + d$ breakup. The VMC and SM cross sections agree, due primarily to the similarity of the (dominant) spectroscopic factor to the 1^+ final state. Both calculations over-predict the measured cross section of 30.7(18) mb.

Assuming isospin symmetry, the spectroscopic factors of the 0^+ states in ^{6}Li and ^{6}He (isobaric analogs) and the measured ^{6}He(0^+) experimental cross section [13.3(5) mb] predict a cross section of 6.7 mb to ^{6}Li(0^+) and, consequently, that about 24.0 mb of the inclusive cross section leads to the 1^+ ground state. The theoretical 1^+ state cross section is of order 40 mb, suggesting that the reaction model also overpredicts the cross sections to both ^{6}Li final states. A future measurement is planned to quantify these individual cross sections exclusively using coincident γ-ray spectroscopy.

B. Knockout reactions from $A = 9$

A study of the mirror reactions (^{9}Li,^{8}Li) and (^{9}C,^{8}B) was performed combining the present neutron knockout data from ^{9}Li and previous proton knockout data from ^{9}C. Cross sections from ^{9}C to ^{8}B were determined in two previous experiments at 100 MeV/u and the results, 56(3) mb [12] and 54(4) mb [36], were in excellent agreement. In the present experiment, two independent inclusive cross-section measurements from ^{9}Li to ^{8}Li were performed at 80 MeV/u using two different target materials and thicknesses. For the Be and C targets the deduced inclusive cross sections were 55.6(29) mb and 63(4) mb, respectively. Parallel momentum distributions obtained using both targets and the resulting fits are presented in Fig. 5.

For proton knockout from ^{9}C the calculated VMC inclusive cross section is 64.4(15) mb in reasonable agreement with the 56(3) mb obtained experimentally. For the mirror reaction,

TABLE IV. Comparison of theoretical and experimental inclusive cross sections for knockout reactions from A = 9 projectiles. The spectroscopic factors (SF) from shell-model include the 1.13 center-of-mass motion correction.

Reaction	Final state	SF CKPOT	SF VMC	σ_{th}^{SM} (mb)	σ_{th}^{VMC} (mb)	σ_{exp} (mb)
(^{9}Li,^{8}Li)	2^+	0.909	1.103	47.3	56.3(11)	
	1^+	0.363	0.460	17.3	22.1(6)	
Inclusive				64.6	78.4(13)	55.6(29)[a]
(^{9}C,^{8}B)	2^+	0.909	1.103	55.7	64.4(15)	
Inclusive				55.7	64.4(15)	56(3)[b]

[a]Results using the Be reaction target.
[b]Experimental result from Ref. [12].

with neutron separation energy 4.06 MeV, the theoretical analysis included both the 2^+ ground state and the bound-excited 1^+ state at 981 keV in ^{8}Li. Differences between the VMC the SM spectroscopic factors (see Table IV) result in a 20% difference in their cross sections, the VMC giving 78.4(13) mb. This is to be compared to the experimental values of 55.6(29) mb and 63(4) mb from the Be and C targets.

In terms of mirror symmetry it is of particular interest that the measured (^{9}C,^{8}B) and (^{9}Li,^{8}Li) cross sections, of 56(3) mb and 55.6(29) mb, are essentially equal, despite there being an additional bound excited state in ^{8}Li. Theoretically, this mirror symmetry is reflected in the spectroscopic factors that are identical for the 2^+ state overlaps. Neutron removal to the 1^+ excited state is calculated to produce about 20 mb of additional cross section that seems absent from the proton knockout experiment. The experimental cross sections being the same suggests either (a) a redistribution of strength between the two states in ^{8}Li or (b) if the 2^+ state cross sections are symmetric, that the 1^+ state spectroscopic factor is overpredicted. An exclusive measurement would be necessary to discriminate between these two possibilities. As is discussed below, a very similar observation was made for the $A = 10$ mirror reaction that was also studied.

C. Knockout reactions from $A = 10$

The (^{10}C,^{9}C) and (^{10}Be,^{9}Be) neutron knockout reactions were the main focus of an earlier study [10]. These reactions were performed using two different settings of the beam energy or the target materials to explore possible systematic effects and to ensure consistency of the final results. For neutron removal from ^{10}C, the cross section was measured using both Be and C reaction targets at 120 MeV/u. The neutron knockout from ^{10}Be was performed at beam energies of 80 and 120 MeV/u using the ^{9}Be reaction target. The influence of the choice of target and beam energy was found to have a minimal impact on the deduced experimental cross sections.

The (^{10}Be,^{9}Li) proton knockout reaction, the mirror reaction to (^{10}C,^{9}C), was also studied in the same experiment. This reaction was studied at 80 MeV/u on the ^{9}Be reaction target. The measured inclusive cross section from the parallel momentum distribution in Fig. 5 was 26.0(13) mb. The (^{10}Be,^{9}Li) reaction can populate the $\frac{3}{2}^-$ ground state and the $\frac{1}{2}^-$, 2.69 MeV, excited state of ^{9}Li. Similarly to the other $A = 10$ cases, the VMC and SM spectroscopic factors differ by up to a factor of 2. The inclusive cross sections are shown in Table V. The VMC- and SM-derived theoretical values, of 50.3(31) mb and 61.8 mb, overpredict the experimental value of 26.0(13) mb.

TABLE V. Comparison of theoretical and experimental inclusive cross sections for knockout reactions from A = 10 projectiles. The spectroscopic factors (SF) from shell-model include the 1.11 center-of-mass motion correction.

Reaction	Final state	SF CKPOT	SF VMC	σ_{th}^{SM} (mb)	σ_{th}^{VMC} (mb)	σ_{exp} (mb)
(^{10}Be,^{9}Li)	$\frac{3}{2}^-$	1.929	1.043	54.2	36.3(30)	
	$\frac{1}{2}^-$	0.282	0.434	7.6	14.0(9)	
Inclusive				61.8	50.3(31)	26.0(13)
(^{10}C,^{9}C)	$\frac{3}{2}^-$	1.933	1.043	48.1	32.8(20)	
Inclusive				48.1	32.8(20)	23.4(11)[a]
(^{10}Be,^{9}Be)	$\frac{3}{2}^-$	2.622	1.932	102.2	73(5)	
Inclusive				102.2	73(5)	71(4)[b]

[a]Results using the Be reaction target.
[b]Results at an incident beam energy of 120 MeV/u.

The VMC and SM theoretical cross sections for the (^{10}C,^{9}C) reaction show even larger differences than for (^{10}Be,^{9}Li). The VMC cross section is 32.8(20) mb compared to the 23.4(11) mb obtained experimentally. The VMC cross section for the (^{10}Be,^{9}Be) neutron knockout reaction, of 73(5) mb is in agreement with the experimental result of 71(4) mb.

Similarly to the mass $A = 9$ mirror reactions, the (^{10}C,^{9}C) and (^{10}Be,^{9}Li) experimental cross sections, of 23.4(11) and 26.0(13) mb, are essentially identical. Although in this case the beam energies differed, cross-section changes between 80 and 120 MeV/u are small. The size of this effect was already shown in Table I, for (^{10}Be,^{9}Be), performed at the two energies. These first *mirror* single-nucleon knockout reaction measurements have thus identified an interesting symmetry in the measured inclusive cross sections. As for the $A = 9$ nuclei discussion, an exclusive measurement is necessary to determine and understand these ^{9}Li final-state populations. It would also be desirable to extend the experimental data on mirror knockout reactions to additional and heavier systems.

V. SUMMARY OF RESULTS

A graphical comparison of the theoretical and experimental inclusive cross sections is presented in Fig. 9 for the seven reactions studied in this work. Reactions are organized according to projectile mass and the type (proton or neutron) of nucleon removed. The mass $A = 9$ and 10 mirror reactions are displayed in the center panels.

The (^{7}Li,^{6}Li) neutron knockout and (^{7}Li,^{6}He) proton knockout reactions were the lightest projectile cases studied. The VMC structure inputs, included within the reaction model, were unable to describe the experimental inclusive cross sections quantitatively. While the VMC overlaps will take account of the major structural changes between the initial and

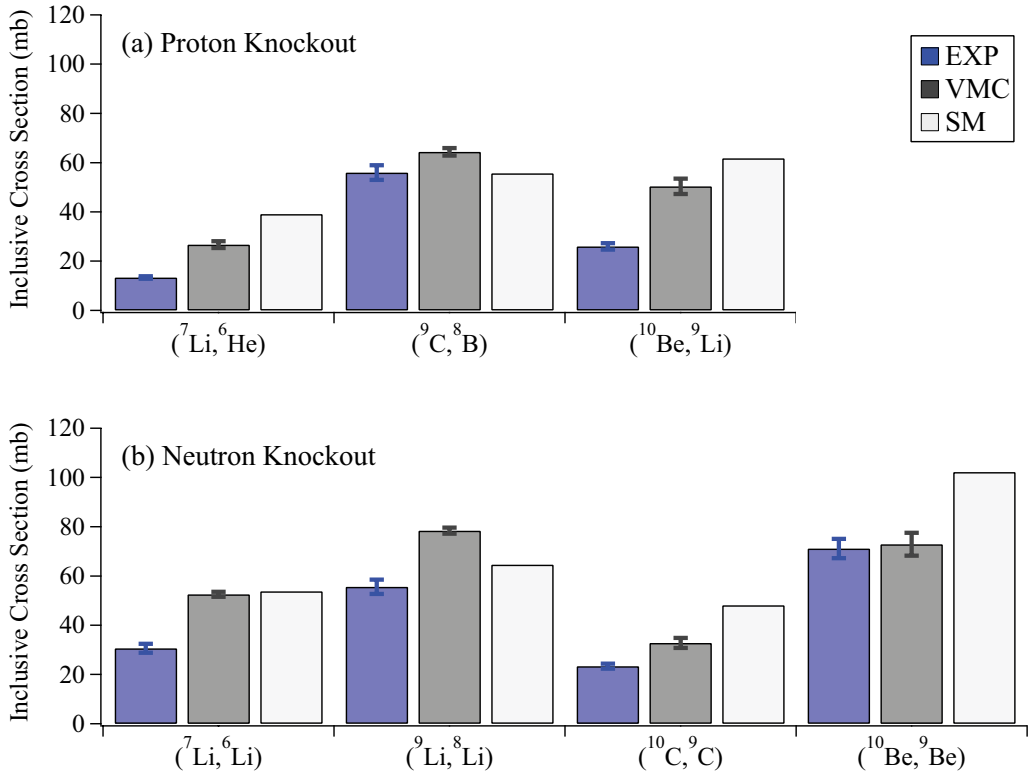

FIG. 9. (Color online) Comparison of the SM and VMC theoretical results to the inclusive knockout cross sections for the reactions studied in this work. Experimental results for (^{9}C,^{8}B) are from Ref. [12].

final states, as, e.g., reflected in the large difference between in the VMC and SM spectroscopic factors for (^{7}Li,^{6}He), the weakly bound cluster and halolike degrees of freedom of the ^{6}Li and ^{6}He residues are not present in the reaction dynamics description. This is a severe limitation of the present model description for such light and few-body systems. An exclusive cross-section measurement for the 0^{+} state population in ^{6}Li, when combined with the present measurement, could provide an additional probe of the role of mirror symmetry and the importance of (nonspectator) residue degrees of freedom in this case.

The measured cross sections for the mirror reaction pairs (^{9}C,^{8}B)/(^{9}Li,^{8}Li) and (^{10}Be,^{9}Li)/(^{10}C,^{9}C), the first such pairs studied with this technique, were found to be essentially identical in each mirror pair. This is a surprising result since, theoretically, the presence of an additional excited final state on the neutron-rich sides, i.e., in ^{8}Li and ^{9}Li, increases the calculated inclusive cross sections for these channels. For these cases, VMC predicts an additional 22 and 14 mb of cross section to these excited states in ^{8}Li and ^{9}Li, respectively. This additional excited states yield should have been observed in the experiment, based on the VMC spectroscopic factors. The (^{9}C,^{8}B) and (^{10}C,^{9}C) experimental cross sections were reasonably well reproduced by the VMC inputs. The nucleon separation energies for these latter cases are 1.3 and 21.3 MeV, respectively, corresponding to the two extremes in the present study. The differences between the VMC and SM inclusive cross sections are dominated by the spectroscopic factors calculated by these models.

This impact of the spectroscopic factors is also seen clearly in the (^{10}Be,^{9}Be) channel. In Table II there are (geometric) differences between both the residue and overlap rms radii computed using the VMC and SM methods but, as was discussed using Fig. 8, these differences then conspire to produce nearly identical values for the single-particle cross sections. The differences in the theoretical cross sections thus arise essentially from the different spectroscopic factors of 1.93 and 2.62 from the VMC and SM calculations, respectively. The experimental result for this case is in good agreement with VMC.

In general, the VMC densities and overlaps provide a reasonable agreement with many of the new data values. Specific cases that agree less well quantitatively are (a) the $A = 7$ cases, where the rather unique few-body cluster and halolike degrees of freedom of the residues are neglected in the reaction description and (b) the (^{9}Li,^{8}Li) and (^{10}Be,^{9}Li) cases, where the VMC calculations for the ground-state transitions are only a closer match with the experimental values. A more detailed assessment of the VMC-derived residue ground- and excited-states spectroscopic factors in these cases would require the different particle-bound final-state yields to be measured exclusively.

VI. CONCLUSION

A systematic study of single-nucleon removal reactions from p-shell nuclei has been performed using intermediate-

energy secondary beams. A detailed comparison was made of new experimental inclusive cross-section data with theoretical predictions based on variational Monte Carlo wave functions and structure inputs to the reactions. The reaction model was modified to accept the residue densities and projectile-residue overlaps calculated using the AV-18 two-body and UIX three-body interactions. The cross sections obtained using shell-model and Hartree-Fock structure inputs, as have been developed and used for more massive nuclei, were also presented for comparison purposes. The VMC calculations were found to provide a reasonable quantitative description of the experimental data for several reactions where nucleons with large separation energies were removed but did not describe some of the more weakly bound nucleon removal cases with comparable accuracy.

For the two pairs of mirror reactions, (^{10}C,^{9}C)/(^{10}Be,^{9}Li) and (^{9}C,^{8}B)/(^{9}Li,^{8}Li), the measured inclusive cross sections were found to agree for each pair. This is despite there being an additional bound state in the ^{8}Li and ^{9}Li residues that, given the theoretical spectroscopic factors, are predicted to be populated with significant additional cross section. Experimentally, it is of great interest to expand the study of these mirror reactions with exclusive measurements using γ-ray spectroscopy to compare the populations of the individual final states.

An extension of this work to knockout studies with the heaviest, mass $A = 11$ and 12, p-shell projectiles, including the exploration of mirror reactions using final-state exclusive measurements—in parallel to improvements in the *ab initio* nuclear-structure models—promise important steps towards an improved understanding of the microscopic structure of p-shell nuclei.

ACKNOWLEDGMENTS

The authors acknowledge the insight and stimulus contributed by the late Gregers Hansen to the proposal for this study. This work was supported by the National Science Foundation under Grants No. PHY-0606007 and No. PHY-1068217, the United Kingdom Science and Technology Facilities Council (STFC) under Grants No. ST/F012012 and No. ST/J000051, and the US Department of Energy Office of Nuclear Physics under Contract No. DE-AC02-06CH11357 and SciDAC Grant No. DE-FC02-07ER41457.

[1] S. C. Pieper and R. B. Wiringa, Annu. Rev. Nucl. Part. Sci. **51**, 53 (2001).
[2] P. Navrátil, S. Quaglioni, I. Stetcu, and B. R. Barrett, J. Phys. G: Nucl. Part. Phys. **36**, 083101 (2009).
[3] E. A. McCutchan *et al.*, Phys. Rev. Lett. **103**, 192501 (2009).
[4] P. Mueller *et al.*, Phys. Rev. Lett. **99**, 252501 (2007).
[5] M. Brodeur *et al.*, Phys. Rev. Lett. **108**, 052504 (2012).
[6] A. H. Wuosmaa *et al.*, Phys. Rev. C **72**, 061301(R) (2005).
[7] A. H. Wuosmaa *et al.*, Phys. Rev. Lett. **94**, 082502 (2005).
[8] A. H. Wuosmaa *et al.*, Phys. Rev. C **78**, 041302(R) (2008).
[9] L. Lapikás, J. Wesseling, and R. B. Wiringa, Phys. Rev. Lett. **82**, 4404 (1999).
[10] G. F. Grinyer *et al.*, Phys. Rev. Lett. **106**, 162502 (2011).
[11] B. A. Brown, P. G. Hansen, B. M. Sherrill, and J. A. Tostevin, Phys. Rev. C **65**, 061601 (2002).
[12] D. Bazin *et al.*, Phys. Rev. Lett. **102**, 232501 (2009).
[13] D. J. Morrissey, B. M. Sherrill, M. Steiner, A. Stolz, and I. Wiedenhoever, Nucl. Instrum. Methods B **204**, 90 (2003).
[14] D. Bazin, J. A. Caggiano, B. M. Sherrill, J. Yurkon, and A. Zeller, Nucl. Instrum. Methods B **204**, 629 (2003).
[15] M. Berz, K. Joh, J. A. Nolen, B. M. Sherrill, and A. F. Zeller, Phys. Rev. C **47**, 537 (1993).
[16] C. A. Bertulani and P. G. Hansen, Phys. Rev. C **70**, 034609 (2004).
[17] A. Gade *et al.*, Phys. Rev. C **71**, 051301(R) (2005).
[18] S. McDaniel *et al.*, Phys. Rev. C **81**, 024301 (2010).
[19] F. Flavigny, A. Obertelli, A. Bonaccorso, G. F. Grinyer, C. Louchart, L. Nalpas, and A. Signoracci, Phys. Rev. Lett. **108**, 252501 (2012).
[20] J. A. Tostevin, J. Phys. G **25**, 735 (1999).
[21] J. A. Tostevin, Nucl. Phys. A **682**, 320c (2001).
[22] P. G. Hansen and J. A. Tostevin, Annu. Rev. Nucl. Part. Sci. **53**, 219 (2003).
[23] L. Ray, Phys. Rev. C **20**, 1857 (1979).
[24] A. Gade *et al.*, Phys. Rev. C **77**, 044306 (2008).
[25] B. A. Brown, Phys. Rev. C **58**, 220 (1998).
[26] C. J. Horowitz, S. J. Pollock, P. A. Souder, and R. Michaels, Phys. Rev. C **63**, 025501 (2001).
[27] B. A. Brown, S. Typel, and W. A. Richter, Phys. Rev. C **65**, 014612 (2001).
[28] R. B. Wiringa, V. G. J. Stoks, and R. J. Schiavilla, Phys. Rev. C **51**, 38 (1995).
[29] B. S. Pudliner, V. R. Pandharipande, J. Carlson, and R. B. Wiringa, Phys. Rev. Lett. **74**, 4396 (1995).
[30] S. C. Pieper, AIP Conf. Proc. **1011**, 143 (2008).
[31] I. Brida, S. C. Pieper, and R. B. Wiringa, Phys. Rev. C **84**, 024319 (2011).
[32] K. M. Nollett and R. B. Wiringa, Phys. Rev. C **83**, 041001(R) (2011).
[33] W. Nörtershäuser, T. Neff, R. Sánchez, and I. Sick, Phys. Rev. C **84**, 024307 (2011).
[34] R. B. Wiringa and R. Schiavilla, Phys. Rev. Lett. **81**, 4317 (1998).
[35] S. Cohen and D. Kurath, Nucl. Phys. **71**, 1 (1965).
[36] J. Enders *et al.*, Phys. Rev. C **67**, 064301 (2003).